

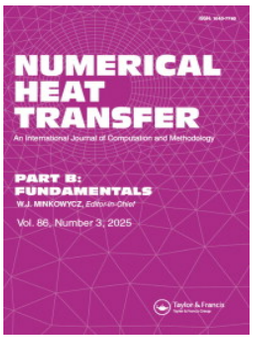
https://dspace.org/

Computational investigation for silicamolybdenum disulfidewaterbased hybrid nanofluid over an exponential stretching sheet with spectral quasilinearization method

M Shamshuddin; Titilayo Agbaje; K Asogwa; Katta Ramesh

TAYLOR & FRANCIS INC
https://hdl.handle.net/10539/47314
WOS

Downloaded from a DSpace repository. https://dspace.org/



Taylor & Francis
Taylor & Francis Group

Numerical Heat Transfer, Part B: Fundamentals
An International Journal of Computation and Methodology

ISSN: 1040-7790 (Print) 1521-0626 (Online) Journal homepage: www.tandfonline.com/journals/unhb20

Computational investigation for silica-molybdenum disulfide/water-based hybrid nanofluid over an exponential stretching sheet with spectral quasi-linearization method

MD. Shamshuddin, T. M. Agbaje, K. K. Asogwa & Katta Ramesh

To cite this article: MD. Shamshuddin, T. M. Agbaje, K. K. Asogwa & Katta Ramesh (2025) Computational investigation for silica-molybdenum disulfide/water-based hybrid nanofluid over an exponential stretching sheet with spectral quasi-linearization method, Numerical Heat Transfer, Part B: Fundamentals, 86:3, 537-561, DOI: 10.1080/10407790.2023.2289503

To link to this article: https://doi.org/10.1080/10407790.2023.2289503

Published online: 11 Dec 2023.

Submit your article to this journal

Article views: 125

View related articles

View Crossmark data

Citing articles: 9 View citing articles

Full Terms & Conditions of access and use can be found at
https://www.tandfonline.com/action/journalInformation?journalCode=unhb20

NUMERICAL HEAT TRANSFER, PART B: FUNDAMENTALS
2025, VOL. 86, NO. 3, 537–561
https://doi.org/10.1080/10407790.2023.2289503

Taylor & Francis
Taylor & Francis Group

Check for updates

Computational investigation for silica-molybdenum disulfide/water-based hybrid nanofluid over an exponential stretching sheet with spectral quasi-linearization method

MD. Shamshuddin[a], T. M. Agbaje[b], K. K. Asogwa[c], and Katta Ramesh[d,e]

[a]Department of Computer Science and Artificial Intelligence (Mathematics), SR University, Warangal, Telangana, India; [b]School of Computer Science and Applied Mathematics, University of the Witwatersrand, Johannesburg, South Africa; [c]Department of Mathematics, Nigeria Maritime University, Okerenkoko, Delta State, Nigeria; [d]Department of Pure and Applied Mathematics, School of Mathematical Sciences, Sunway University, Petaling Jaya, Selangor Darul Ehsan, Malaysia; [e]Department of Mathematics, Graphic Era (Deemed to be University), Dehardun, Uttarakhand, India

ABSTRACT

The current research is focused on analyzing gyrotactic microorganisms within a hybridized nanofluid (NF) model by considering magnetohydrodynamics, electroosmosis, and radiation effects. Demarcated flow is mathematically modeled to yield coupled nonlinear partial differential equations, which are consequently transmuted into ordinary differential equations (ODEs) by adopting similarity transformations. The spectral quasilinearization method is used to generate the solutions of the transformed ODEs *via* MATLAB. The influence of various flow parameters on both mono NF and hybrid NF phases for velocity, thermal, concentration, and density of motile microorganism is depicted using graphs. The convergence and residual errors are demonstrated in tables for various influenced parameters on hybrid NF. Additionally, interested physical quantities like shear stress and rate of thermal diffusion at the wall have been tabulated by varying the controlling parameters. It is concluded from the current analysis that the higher velocities and temperatures are observed in hybrid NF model as compared with the mono NF model. Biot number and Hartmann number enhance the temperature profile. The velocity is an enhancing function of mixed convection parameter and bioconvection Rayleigh constant. NF flow over a stretching sheet finds applications in enhancing heat transfer for efficient cooling systems, such as electronics and solar collectors, as well as improving drug delivery in biomedicine, nanoparticle synthesis, and chemical processes.

ARTICLE HISTORY
Received 5 June 2023
Revised 22 November 2023
Accepted 26 November 2023

KEYWORDS
Computational scrutinization; gyrotactic microorganisms; hybrid nanofluids; metallic nanoparticles; stretching sheet

1. Introduction

The research of nanoparticles (NPs) is gaining the fascination of scientists internationally. NPs vary in size from 1 to 100 nm. NPs exhibited increasing interactivity in various science and technology eras with a boost in thermal conductivity. NPs are chosen over fundamental materials as an energy source. The NP volume percentage is typically 1–4%. Choi [1] was the first to characterize nanostructures' remarkable features. NPs serve a significant purpose in the field of

CONTACT Katta Ramesh ramesh.katta1@gmail.com Department of Pure and Applied Mathematics, School of Mathematical Sciences, Sunway University, Petaling Jaya, Selangor Darul Ehsan, Malaysia.

© 2023 Taylor & Francis Group, LLC

Nomenclature

u, v	Velocity components (ms^{-1})	D_m	Diffusivity of microorganisms ($m^2\ s^{-1}$)
x, y	Axial and transverse coordinates (m)	b^*	Chemotaxis constant (m^{-1})
ρ_{hnf}	Density of ternary nanofluid (kg m^{-3})	We	Maximum cell swimming speed (m s^{-1})
μ_{hnf}	Viscosity of ternary nanofluid (kg $m^{-1}\ s^{-1}$)	Pr	Prandtl number
		M	Modified Hartmann number
g	Gravitational force term (m s^{-2})	λ	Mixed convection parameter
T	Temperature (K)	Nr	Buoyancy ratio constant
ρ_p	Density of nanoparticles (kg m^{-3})	Rb	Bioconvection Rayleigh constant
ρ_f	Density of fluid (kg m^{-3})	Rn	Radiation parameter
C	Concentration (g mol^{-1})	Nb	Brownian motion parameter
ρ_m	Density of motile organisms (kg m^{-3})	Nt	Thermophoresis parameter
N	Concentration of microorganisms (g mol^{-1})	Le	Lewis number
		Pe	Peclet number
c_p	Specific heat (J $kg^{-1}\ K^{-1}$)	Lb	Bioconvection Lewis number
k_{hnf}	Thermal conductivity (W $m^{-1}\ K^{-1}$)	δ	Microorganisms' concentration difference parameter
D_B	Brownian motion parameter ($m^2\ s^{-1}$)		
D_T	Thermophoresis parameter (K^{-1})		

medicine, including the treatment of diseases caused by heat and malignancy. Ahmed *et al.* [2] studied the erratic behavior of Maxwell nanoliquid. In accordance with their conclusion, Joule dissipation significantly improves thermal distribution. Using the least square approach, Usman *et al.* [3] discussed the thermal transmission features of NPs along a linked path. According to their findings, the increased volume fraction of NPs diminished temperature dispersion. Asogwa *et al.* [4] investigated the effect of NPs on the surface of an electromagnetic plate. Uddin *et al.* [5] discussed the nanofluid (NF) flow due to a stretching/shrinking sheet with numerical scheme. Uddin *et al.* [6] analyzed the power-law NF motion past a needle in a Darcy porous medium using bvp4c technique. Amirsom *et al.* [7] presented the 3D motion of bioconvective NFs over a bi-axial stretching sheet using bvp4c code. According to Raza *et al.* [8], the significant thermophysical behavior of NPs make them a potent, accessible, reliable source of energy. Other relevant publications are can be seen in Refs. [9–13].

Silica (SiO_2) is the predominant component of sand. Silica as a NP constitutes one of the most intricate and important families, appearing as both an organic compound and an artificial material. Quartz is a widespread form of silica (silicon dioxide). It is utilized in structural materials, microchips (as electrical insulators), and dietary and medicinal products. Bhatti *et al.* [14] explored the dynamics of diamond and SiO_2 NPs embedded in a water over an infinitely elastic interface. They discovered that diamond and silica NPs significantly boost the pattern of velocity, while permeability parameter's strong interaction. The Nusselt value decreases as the field of magnetism and porosity measure grow. Ruhani *et al.* [15] swotted the motion of a Newtonian NF comprised of silica-ethylene glycol/water. Iftikhar *et al.* [16] studied the magnetohydrodynamic (MHD) transport of copper and silica NF blends in four irregular tube configurations. They discovered that the heat transmission coefficient has a greater effect on copper-silica NF mixtures than mono-NF. Patil *et al.* [17] evaluated silica and molybdenum disulfide NPs added to water to form a hybrid nanoliquid and reported the pattern of velocity distribution improves, as the frequency criterion value increases.

Molybdenum disulfide (MoS_2) is an inorganic substance categorized as a dichalcogenide chemical. It is formed of distinct layers of molybdenum and sulfur molecules. Due to its minimal adhesion properties and strength, it is frequently employed as a stabilizer. MoS_2 possesses a minimal level of reactivity and is unaffected by weak acids and oxidants. Molybdenum disulfide nanostructures is usually made up of MoS_2 NPs distributed in liquids containing water. Ali *et al.* [18] explored the motion of MoS_2 NPs in a second-grade fluid with motor oil as the base fluid.

Kumar *et al.* [19] utilized Runge–Kutta–Fehlberg to analyze the consequences of MoS_2 and silver NPs on the motion of a particulate liquid *via* a stretching cylinder and reported that an increase in particle mass concentration decrease both the heat gradient of dust and liquid phases. Arif *et al.* [20] explored the fluid flow comprising evenly distributed MoS_2 and graphene NPs in oil employing the Laplace transform technique. They discovered that molybdenum disulfide NPs transfer of heat faster than graphene NPs. Gul *et al.* [21] reported that an increase in temperature reduces entropy generation in MoS_2 NFs. Shafie *et al.* [22] studied the shape effect of MoS2 NPs of four distinct forms in convective fluid flow in porous media. Zhang *et al.* [23] scientifically organized symmetrical and steady Newtonian molybdenum disulfide NFs. Khan *et al.* [24] studied the fluid flow comprised of silica and MoS_2 to ascertain the influence of a heat source/sink. Saqib *et al.* [25] swotted MHD ethylene glycol-based NFs with molybdenum disulfide NPs. Talha *et al.* [26] studied fractional ferro-NF flow by employing the Laplace transform method. Liu *et al.* [27] performed investigations on the expansion of heat energy with thermal conductivity. Khan *et al.* [28] explored the impact of various geometry factors on the MHD motion of MoS_2 NPs and water as the transporting fluid. They discovered that blade and platelet-shaped molybdenum disulfide NPs exhibited higher transference of heat than cylinder and brick-shaped NPs.

In the contemporary world, experts are creating hybrid or merged NPs to boost or enhance the thermal conductivity of nanomaterials. When nano-meter-sized molecules of two or more separate substances are mixed simultaneously, a new substance known as composite NPs is produced. Hybrid NFs is the name given to the liquids that are produced because of hybrid NPs. These substances are utilized for a variety of purposes, including, but not limited to, the dissipation of heat in automotive engines, electrical parts, and machineries. Hussain [29] investigated the effects of hybrid NF across an expanding sheet while simultaneously creating entropy. They conducted a study on the process of heat transmission while the sunlight was present and found that the hybrid NF performed noticeably better than the traditional NF. Takabi and Salehi [30] computationally investigated spontaneous convection inside the laminar flow regime in a curved enclosure containing NF in the involvement of a discrete heat source. Suresh *et al.* [31] evaluated the viscoelastic hybrid NFs. They revealed that the characteristics of the hybrid NF improve with increasing concentrations of solid volume NPs. Unlike solitary NF, the introduction of hybrid NF permits the drilling flow velocity to be controlled, according to Khan *et al.* [32], who employed a fractional-based framework to reach their result. Furthermore, incorporating a range of NP forms into water was demonstrated to increase the rate of heat transfer by up to 11.149%. The convective heat transfer of a hybrid NF was discussed by Al-Arabi *et al.* [33] in a permeable medium that contained NPs of varying shapes. It was discovered that the friction coefficient of a combination of titanium oxide NF and silver had a higher value than the friction coefficient of titanium oxide NF used on its own. Devi and Devi [34] demonstrated 3D hybrid NF flow as a result of a stretching sheet. Some more relevant studies can be seen through the Refs. [35–39].

In recent years, numerical techniques for solving flow problems have evolved into a significant field of study due to their importance in a variety of scientific and technological disciplines. Typically, fluid dynamic problems are expressed as boundary value problems requiring partial differential equations. Frequently, solving boundary value problems is extraordinarily difficult. Numerous numerical methods exist for solving boundary value problems. The spectral quasi-linearization technique for solving nonlinear differential equations is a highly efficient and trustworthy method. The numerical method described as the spectral quasilinearization method (SQLM) has been utilized over the past 5 years to find numerical solutions to difficulties associated with fluid dynamics, with impressive outcomes and remarkable precision. Using the SQLM, Acharya [40] examined the thermal action and subsequent cooling of a NF spilling on a slanted rotating disk. Comparing the SQLM and the bvp4c method, Ibrahim [41] investigated the influence of second order slip flow on the heat transmission of a NF across an extendable surface. Ansari *et al.* [42] outlined the Jeffrey NF flow over a Riga plate by incorporating the influences of

various effects using a spectral quasilinearization approach. Using the SQLM, Shateyi *et al.* [43] investigated the Carreau–Yasuda NF flow across a stretched surface. Dhlamini *et al.* [44] investigated the 3D flow of a rotating NF comprising microorganisms and a shielded plate traveling in the fluid using spectral quasilinearization.

In view of the aforementioned studies and applications, the authors have motivated to study the propulsion of hybrid NF flow over an exponential stretching sheet under the influences of magnetic field, electroosmosis, thermal radiation, Brownian motion, and thermophoresis. In the current study, the authors have implemented the modified Buongiorno NF model. Using the similarity transformations along with nondimensional quantities the complex system of equations converted to simplified model. The numerical simulations have been provided using SQLM. The graphical results have been provided for various flow quantities with sundry parameters. The current analysis provides the answers of the following research questions:

- How does the velocity of a mixed convection NF flow change with the Hartmann number?
- What is the effect of the Brownian motion parameter on the temperature of a NF flow?
- What is the influence of involved different parameters on the local Nusselt number (LNN) and skin friction coefficient (SFC) in a NF flow?

2. Mathematical modeling

Consider an incompressible hybrid NF (silica-molybdenum disulfide/water) flow over an exponential stretching sheet surface. The MHDs, electroosmosis, gyrotactic microorganisms and radiation have been considered. The x-axis runs along the sheet and y-axis is measured normal to it (see Figure 1). It is also assumed that the surface is maintained at velocity, temperature, concentration, and microorganisms $u_w, T_w, C_w,$ and N_w respectively and the same quantities at the boundary layer region are $u_\infty, T_\infty, C_\infty,$ and N_∞ respectively. The flow is characterized by velocity, which is governed by a randomly expanding surface, and the velocity of the stretching sheet is considered as $u_w(x) = U_0 e^{x/l}$.

The governing equations for assumed problem under the influence of gyrotactic microorganisms, radiation and electromagnetohydrodynamic can be expressed as

$$\frac{\partial u}{\partial x} + \frac{\partial v}{\partial y} = 0, \tag{1}$$

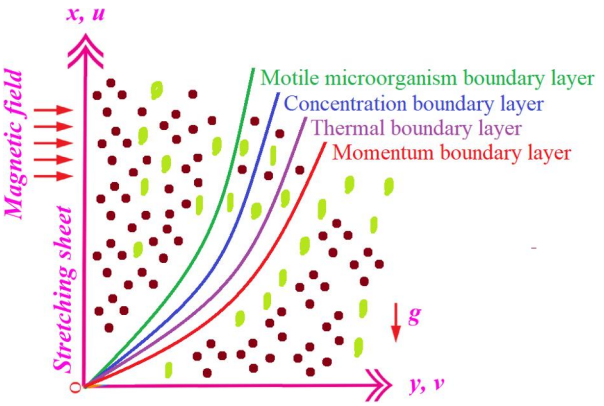


Figure 1. Geometry of flow configuration.

$$\rho_{hnf}\left(u\frac{\partial u}{\partial x}+v\frac{\partial u}{\partial y}\right)=\left.\begin{array}{c}\mu_{hnf}\dfrac{\partial^2 u}{\partial y^2}-\sigma_{hnf}B_0^2u+\rho_eE_x+\\ g\left((1-C_\infty)\ \rho_{hnf}\ \beta_{hnf}(T-T_\infty)-(\rho_p-\rho_f)(C-C_\infty)-\right.\\ \left.(\rho_m-\rho_f)\beta_1(N-N_\infty)\right)\end{array}\right| \tag{2}$$

$$(\rho c_P)_{hnf}\left(u\frac{\partial T}{\partial x}+v\frac{\partial T}{\partial y}\right)=\left(k_{hnf}+\frac{16\ \sigma^*T_\infty^3}{3k^*}\right)\frac{\partial^2 T}{\partial y^2}+(\rho c_P)_p\left(D_B\frac{\partial T}{\partial y}\frac{\partial C}{\partial y}+\frac{D_T}{T_\infty}\left(\frac{\partial T}{\partial y}\right)^2\right)\Bigg\}, \tag{3}$$

$$\left(u\frac{\partial C}{\partial x}+v\frac{\partial C}{\partial y}\right)=D_B\frac{\partial^2 C}{\partial y^2}+\frac{D_T}{T_\infty}\frac{\partial^2 T}{\partial y^2}, \tag{4}$$

$$\left(u\frac{\partial N}{\partial x}+v\frac{\partial N}{\partial y}\right)=D_m\frac{\partial^2 N}{\partial y^2}-\frac{b^*We\ D_T}{(C_w-C_\infty)}\left(\frac{\partial}{\partial y}\left(N\frac{\partial C}{\partial y}\right)\right), \tag{5}$$

with the suitable boundary conditions

$$\left.\begin{array}{c}u=u_w(x),\ \ v=-v_w(x),\ \ -k_{hnf}\dfrac{\partial T}{\partial y}=h_0(T_w(x)-T),\ \ C=C_w,\ \ N=N_w(x)\ \ at\ \ y=0\\ u\to 0,\ \ v\to 0,\ \ T\to T_\infty(x),\ \ C\to C_\infty(x),\ \ N\to N_\infty(x)\ \ at\ \ y\to\infty.\end{array}\right| \tag{6}$$

In which,

$$\left.\begin{array}{c}u_w(x)=U_0\ \ e^{x/l},\ \ T_w(x)=T_\infty+T_0\ \ e^{x/2l},\\ C_w(x)=C_\infty+C_0\ \ e^{x/2l},\ \ N_w(x)=N_\infty+N_0\ \ e^{x/2l}\ .\end{array}\right\}$$

Introduce the following nondimensional quantities and similarity transformations [45]

$$\left.\begin{array}{c}u=U_0e^{\frac{x}{l}}\ f'(\eta),\ \ v=\sqrt{\dfrac{\mu_f\ \ U_0}{2\ \ l\ \ \rho_f}}\ \ e^{x/2l}\ \ \{f(\eta)+\eta\ f'(\eta)\},\ \ \eta=\sqrt{\dfrac{\rho_f\ \ U_0}{2\ \ l\ \ \mu_f}}\ \ e^{x/2l}y,\\ \kappa=2ez\sqrt{\dfrac{n_0\ \ \vartheta_f\ \ l}{\varepsilon_{eff}\ \ k_B\ \ T_v\ \ U_0\ \ e^{2x/l}}},\ \ \theta=\dfrac{T-T_\infty}{T_w-T_\infty},\ \ \sigma=\dfrac{C-C_\infty}{C_w-C_\infty},\ \ \chi=\dfrac{N-N_\infty}{N_w-N_\infty},\\ \lambda=\dfrac{2\ \ l\ \ g\ \ \beta_f(1-C_\infty)(T_w-T_\infty)}{U_0^2\ \ e^{2x/l}},\ \ Nr=\dfrac{(\rho_p-\rho_f)(C_w-C_\infty)}{\rho_f\beta_f\ \ (1-C_\infty)(T_w-T_\infty)},Rb=\dfrac{\beta_1(\rho_m-\rho_f)(N_w-N_\infty)}{\rho_f\beta_f\ \ (1-C_\infty)(T_w-T_\infty)},\\ Bi=\dfrac{h_0}{k_f}\sqrt{\dfrac{2\ \ \mu_f\ \ l}{U_0\ \ \rho_f}}\ \ e^{-x/2l},\ \ Pr=\dfrac{(\mu c_p)_f}{k_f},\ \ Rn=\dfrac{16\ \ \sigma^*T_\infty^3}{3k^*(\mu c_p)_f},\ \ Nb=\dfrac{D_B\ \ (\mu c_p)_p(C_w-C_\infty)}{\vartheta_f\ \ (\mu c_p)_f},\\ Nt=\ \ \dfrac{D_T\ \ (\mu c_p)_p(T_w-T_\infty)}{\vartheta_f\ \ (\mu c_p)_fT_\infty},\ \ U_{hs}=\dfrac{E_x\ \ \zeta\ \ \varepsilon_{eff}}{U_0\ \ \mu_f},\ \ Le=\dfrac{\vartheta_f}{D_B},\ \ Lb=\dfrac{\vartheta_f}{D_m}\\ Pe=\dfrac{b^*We}{D_m},\ \ \delta=\dfrac{N_\infty}{(N_w-N_\infty)}.\end{array}\right\} \tag{7}$$

The expressions φ_1 and φ_2 symbolize the NPs volume fraction of MoS_2 and SiO_2 respectively. s_1, s_2, f, nf, and hnf are used to represent the solid particle of MoS_2, the solid of SiO_2, base

Table 1. Thermophysical characteristics of the base and nanoparticles.

	ρ (Kg/m^3)	c_p (J/Kg K)	k (W/m K)	$\beta\times10^{-5}$ $(K)^{-1}$	σ $(\Omega\ m)^{-1}$
H_2O	997.1	4179	0.613	21	0.05
MoS_2	5060	397.746	34.5	2.8424	2.09×10^4
SiO_2	2650	730	1.5	0.056	1.0×10^{-18}

fluid (H_2O), NF, and hybrid NF. The effective characteristics of NF and hybrid NF are defined as follows, while the physical and thermal characteristics of MoS_2, SiO_2, and H_2O are listed in Table 1 as following [3]

Density: $\frac{\rho_{hnf}}{\rho_f} = (1-\varphi_1)\left\{1-\varphi_1+\varphi_1\left(\frac{\rho_{s1}}{\rho_f}\right)\right\}+\varphi_2\left(\frac{\rho_{s2}}{\rho_f}\right) = H_1,$

Dynamic viscosity: $\frac{\mu_{hnf}}{\mu_f} = \frac{1}{(1-\varphi_1)^{2.5}(1-\varphi_2)^{2.5}} = H_2,$

Thermal expansion coefficient: $\frac{(\rho\beta)_{hnf}}{(\rho\beta)_f} = (1-\varphi_2)\left\{1-\varphi_1+\varphi_1\left(\frac{(\rho\beta)_{s1}}{(\rho\beta)_f}\right)\right\}+\varphi_2\left(\frac{(\rho\beta)_{s2}}{(\rho\beta)_f}\right) = H_3,$

Specific heat: $\frac{(\rho c_p)_{hnf}}{(\rho c_p)_f} = (1-\varphi_2)\left\{1-\varphi_1+\varphi_1\left(\frac{(\rho c_p)_{s1}}{(\rho c_p)_f}\right)\right\}+\varphi_2\left(\frac{(\rho c_p)_{s2}}{(\rho c_p)_f}\right) = H_4,$

Thermal conductivity: $\frac{k_{hnf}}{k_f} = H_5,$ where $\frac{k_{hnf}}{k_f} = \frac{k_{s2}+2k_{nf}-2\varphi_2(k_{nf}-k_{s2})}{k_{s2}+2k_{nf}+2\varphi_2(k_{nf}-k_{s2})}$ and $\frac{k_{nf}}{k_f} = \frac{k_{s1}+2k_f-2\varphi_1(k_f-k_{s1})}{k_{s1}+2k_f+\varphi_1(k_f-k_{s1})}$,

Electrical conductivity: $\frac{\sigma_{hnf}}{\sigma_f} = H_6,$ where $\frac{\sigma_{hnf}}{\sigma_f} = 1+\frac{3\left(\frac{\varphi_1\sigma_1+\varphi_2\sigma_2}{\sigma_f}-(\varphi_1+\varphi_2)\right)}{2+\left(\frac{\varphi_1\sigma_1+\varphi_2\sigma_2}{(\varphi_1+\varphi_2)\sigma_f}\right)-\left(\frac{\varphi_1\sigma_1+\varphi_2\sigma_2}{\sigma_f}-(\varphi_1+\varphi_2)\right)}$

Using the theory, the resulting dimensionless system can be put in the form

$$H_1\left(2f'^2-ff''\right)-H_2f'''+MH_5f'-\kappa^2U_{hs}\exp(-\kappa\eta)-\lambda(H_3\theta-Nr\sigma-Rb\chi)=0, \tag{8}$$

$$H_4\mathrm{Pr}\left(f'\theta-f\theta'\right)-(H_5+Rn\mathrm{Pr})\theta''-Nb\mathrm{Pr}\theta'\sigma'-Nt\mathrm{Pr}\theta'^2=0, \tag{9}$$

$$NbLe\left(f'\sigma-f\sigma'\right)-Nb\sigma''-Nt\theta''=0, \tag{10}$$

$$Lb\left(f'\chi-f\chi'\right)-\chi''+Pe\left((\chi+\delta)\sigma''+\chi'\sigma'\right)=0, \tag{11}$$

with the corresponding boundary conditions

$$\left.\begin{aligned} f(\eta)=0, f'(\eta)=1, H_5\frac{\partial\theta(\eta)}{\partial\eta}=Bi(\theta-1), \sigma(\eta)=1, \chi(\eta)=1 \text{ at } \eta=0,\\ f'(\eta)\to 0, \theta(\eta)\to 0, \sigma(\eta)\to 0, \chi(\eta)\to 0 \text{ at } \eta\to\infty. \end{aligned}\right\} \tag{12}$$

where κ is electroosmosis parameter, Rb is bioconvection Rayleigh constant, U_{hs} is Helmholtz-Smoluchowski velocity, λ is mixed convection parameter, Nr is buoyancy ratio constant, Pr is Prandtl number, Rn is radiation parameter, Le is concentration Lewis number, Pe is Peclet number, δ is nondimensional parameter, Nt is thermophoresis parameter, Lb is bioconvection Lewis number, Nb is Brownian motion parameter, and Bi is Biot number.

3. Parameters of engineering interest

The SFC and the LNN both are considerable quantities can be written as

$$C_{fx}=\frac{\tau_w}{\rho_f u_w^2} \text{ and } Nu_x=-\frac{Lq_w}{k_f(T_w-T_\infty)}, \tag{13}$$

here τ_w is the shear stress of wall and q_w is heat flux from surface to fluid that can be expressed as

$$\tau_w = \mu_{hnf}\left(\frac{\partial u}{\partial y}\right)_{y=0} \text{ and } q_w = k_{hnf}\left(\frac{\partial T}{\partial y}\right)_{y=0}. \tag{14}$$

The dimensionless engineering quantities can be written as

$$\sqrt{\mathrm{Re}_x}C_{fx} = \left(\frac{\mu_{hnf}}{\mu_f}\right)f''(0) \text{ and } \frac{Nu_x}{\sqrt{\mathrm{Re}_x}} = -\left(\frac{k_{hnf}}{k_f}\right)\theta'(0), \tag{15}$$

where $\mathrm{Re}_x = \frac{x^2\rho_f U_0}{2\mu_f l e^{x/l}}$ is the local Reynolds number.

4. Numerical simulations

The governing nonlinear ordinary differential equations given in Eqs. (8)–(11) are solved numerically using the SQLM. The SQLM is a numerical method that employs the Newton-Raphson based linearization method (LM) to linearize the governing equations. The linearized governing equations are thereafter integrated using the Chebyshev spectral method. The SQLM scheme is developed by linearizing the nonlinear terms in the governing equations using Taylor series expansion with the assumption that the difference between the value of unknown function at the current iteration level denoted by $s+1$ and the value of the previous iteration level denoted by s is small. See Ref. [4], for a detailed description of the SQLM. Applying the QLM on the governing equations using one term Taylor series expansion for multiple variables gives:

$$\left.\begin{aligned} a_{0,s}f'''_{s+1} + a_{1,s}f''_{s+1} + a_{2,s}f'_{s+1} + a_{3,s}f_{s+1} + a_{4,s}\theta_{s+1} + a_{5,s}\sigma_{s+1} + a_{4,s}\chi_{s+1} \\ = V_1, \end{aligned}\right\} \tag{16}$$

$$b_{0,s}\theta''_{s+1} + b_{1,s}\theta'_{s+1} + b_{2,s}\theta_{s+1} + b_{3,s}f'_{s+1} + b_{4,s}f_{s+1} + b_{5,s}\sigma'_{s+1} = V_2, \} \tag{17}$$

$$c_{0,}\sigma''_{s+1} + c_{1,s}\sigma'_{s+1} + c_{2,s}\sigma_{s+1} + c_{3,s}f'_{s+1} + c_{4,s}f_{s+1} + c_{5,s}\theta''_{s+1} = V_3, \} \tag{18}$$

$$\left.\begin{aligned} d_{0,s}\chi''_{s+1} + d_{1,s}\chi'_{s+1} + d_{2,s}\chi_{s+1} + d_{3,s}f'_{s+1} + d_{4,s}f_{s+1} + d_{5,s}\sigma''_{s+1} + d_{6,s}\sigma'_{s+1} \\ = V_4, \end{aligned}\right\} \tag{19}$$

where $a_{i,s}$, $b_{i,s}$, $c_{i,s}$, and $d_{i,s}(i = 1, 2, 3, \ldots)$ are known from the previous calculations and are given as:

$$\left.\begin{gathered} a_{0,s} = -H_2,\ a_{1,s} = -H_1 f_s,\ a_{2,s} = 4H_1 f_s' + MH_5,\ a_{3,s} = -H_1 f_s'', \\ a_{4,s} = -\lambda H_3,\ a_{5,s} = \lambda Nr,\ a_{6,s} = \lambda Rb, \\ b_{0,s} = -H_5 - RnPr,\ b_{1,s} = -H_4 Prf_s - NbPr\sigma_s' - 2NtPr\theta_s', \\ b_{2,s} = H_4 Prf_s',\ b_{3,s} = H_4 Pr\theta_s,\ b_{4,s} = -H_4 Pr\theta_s',\ b_{5,s} = -NbPr\theta_s', \\ c_{0,s} = -Nb,\ c_{1,s} = -NbLef_s,\ c_{2,s} = NbLef_s',\ c_{3,s} = NbLe\sigma_s,\ c_{4,s} = -NbLe\sigma_s', \\ c_{5,s} = -Nt, \\ d_{0,s} = -1,\ d_{1,s} = -Lbf_s + Pe\sigma_s',\ d_{2,s} = Lbf_s' + Pe\sigma_s'',\ d_{3,s} = Lb\chi_s, \\ d_{4,s} = -Lb\chi_s',\ d_{5,s} = Pe\chi_s + Pe\delta,\ d_{6,s} = Pe\sigma_s'. \end{gathered}\right\} \tag{20}$$

The right-hand side of Eqs. (16)–(18), are given as:

$$\left.\begin{gathered} V_1 = 2H_1(f_s')^2 - H_1 f_s f_s'' + \kappa^2 U_{hs}\exp(-\kappa\eta), \\ V_2 = H_4 Prf_s'\theta_s - H_4 Prf_s\theta_s' - NbPr\theta_s'\sigma_s' - NtPr(\theta_s')^2, \\ V_3 = NbLef_s'\sigma_s - NbLef_s\sigma_s', \\ V_4 = Lbf_s'\chi_s - Lbf_s\chi_s' + Pe\chi_s\sigma_s'' + Pe\chi_s'\sigma_s'. \end{gathered}\right\} \tag{21}$$

Equations (16)–(19) form the iterative scheme for the SQLM and the equations are solved using the Chebyshev spectral collocation method. Using a suitable initial approximation, which is chosen as a function that satisfy the boundary conditions given in Eq. (12), the iterative scheme in Eqs. (16)–(19), are solved iteratively for f_{s+1}, θ_{s+1}, σ_{s+1}, and χ_{s+1}, for $r = 0, 1, 2, \ldots$. To solve Eqs. (16)–(19), we apply discretization first on the equations using the Chebyshev spectral method. The Chebyshev spectral method is applied on the interval $[-1, 1]$. For ease of the numerical computations, it is important to convert the semi-infinite $[0, \infty)$ to a computational $[0, L]$, where L is an infinite number chosen to be very large. The transformation $\frac{1}{2}L(\zeta + 1)$ is used to convert the interval $[0, L]$ to $[-1, 1]$. We introduce the differentiation matrix $\boldsymbol{D}$ to approximate the unknown variables $f(\eta)$, $\theta(\eta)$, $\sigma(\eta)$, and $\chi(\eta)$ at the collocation points as a matrix vector product, that is:

$$\left.\begin{aligned}
\frac{\partial f}{\partial \eta} &= \sum_{j=0}^{N_x} \boldsymbol{D}_{jk} f(\zeta j) = \boldsymbol{D}F, \quad k = 0, 1, \ldots N_x, \\
\frac{\partial \sigma}{\partial \eta} &= \sum_{j=0}^{N_x} \boldsymbol{D}_{jk} \sigma(\zeta j) = \boldsymbol{D}\sigma, \quad k = 0, 1, \ldots N_x, \\
\frac{\partial \theta}{\partial \eta} &= \sum_{j=0}^{N_x} \boldsymbol{D}_{jk} \theta(\zeta j) = \boldsymbol{D}\Theta, \quad k = 0, 1, \ldots N_x, \\
\frac{\partial \chi}{\partial \eta} &= \sum_{j=0}^{N_x} \boldsymbol{D}_{jk} \chi(\zeta j) = \boldsymbol{D}\chi, \quad k = 0, 1, \ldots N_x,
\end{aligned}\right\} \tag{22}$$

where N_x is the number of collocation points, $\boldsymbol{D} = \frac{2D}{L}$ and

$$\left.\begin{aligned}
f &= \left[F(\zeta_0), \ F(\zeta_1), \ldots, F\left(\zeta_{N_x}\right)\right]^T, \\
\Theta &= \left[\theta(\zeta_0), \ \theta(\zeta_1), \ldots, \theta\left(\zeta_{N_x}\right)\right]^T, \\
\sigma &= \left[\sigma(\zeta_0), \ \sigma(\zeta_1), \ldots, \sigma\left(\zeta_{N_x}\right)\right]^T, \\
\chi &= \left[\chi(\zeta_0), \ \chi(\zeta_1), \ldots, \chi\left(\zeta_{N_x}\right)\right]^T,
\end{aligned}\right\}$$

is a vector function at the collocation points, higher order derivatives are obtained as powers of $\boldsymbol{D}$, that is

$$\left.\begin{aligned}
F^p(\eta) &= \boldsymbol{D}^p F, \\
\Theta^p(\eta) &= \boldsymbol{D}^p \Theta, \\
\sigma^p(\eta) &= \boldsymbol{D}^p \sigma, \\
\chi^p(\eta) &= \boldsymbol{D}^p \chi,
\end{aligned}\right\} \tag{23}$$

where p is the order of the derivative and matrix $\boldsymbol{D}$ is of size $(N_x + 1) \times (N_x + 1)$. Applying the spectral method to the iterative scheme given in Eqs. (16)–(19), and expressing it in matrix form gives

$$\begin{bmatrix} A_{11} & A_{12} & A_{13} & A_{14} \\ A_{21} & A_{22} & A_{23} & A_{24} \\ A_{31} & A_{32} & A_{33} & A_{34} \\ A_{41} & A_{42} & A_{43} & A_{44} \end{bmatrix} \begin{bmatrix} F_{s+1} \\ \Theta_{s+1} \\ \sigma_{s+1} \\ \chi_{s+1} \end{bmatrix} = \begin{bmatrix} V_1 \\ V_2 \\ V_3 \\ V_4 \end{bmatrix}, \tag{24}$$

where A_{ij} and $V_i (i = j = 1, 2, 3, 4)$ are $(N_x + 1) \times (N_x + 1)$ matrices and $(N_x + 1) \times 1$ vectors respectively, defined as

$$\left.\begin{array}{c}
\boldsymbol{A}_{11} = a_{0,s}\boldsymbol{D}^3 + diag[a_{1,s}]_d\boldsymbol{D}^2 + diag[a_{2,s}]_d D + diag[a_{3,s}]_d, \\
\boldsymbol{A}_{12} = [a_{4,s}]_d I, \\
\boldsymbol{A}_{13} = [a_{5,s}]_d I, \\
\boldsymbol{A}_{14} = [a_{6,s}]_d I, \\
\\
\boldsymbol{A}_{21} = diag[b_{3,s}]_d D + diag[b_{4,s}]_d, \\
\boldsymbol{A}_{22} = b_{0,s}\boldsymbol{D}^2 + diag[b_{1,s}]_d D + diag[b_{2,s}]_d, \\
\boldsymbol{A}_{23} = diag[b_{5,s}]_d D, \\
\boldsymbol{A}_{24} = 0, \\
\boldsymbol{A}_{31} = diag[c_{3,s}]_d D + diag[c_{4,s}]_d, \\
\boldsymbol{A}_{32} = c_{5,s}\boldsymbol{D}^2, \\
\boldsymbol{A}_{33} = c_{0,s}\boldsymbol{D}^2 + diag[c_{1,s}]_d D + iag[c_{3,s}]_d, \\
\boldsymbol{A}_{34} = 0, \\
\boldsymbol{A}_{41} = diag[d_{3,s}]_d D + diag[d_{4,s}]_d, \\
\boldsymbol{A}_{42} = 0, \\
\boldsymbol{A}_{43} = diag[d_{5,s}]_d\boldsymbol{D}^2 + diag[d_{6,s}]_d D, \\
\boldsymbol{A}_{44} = d_{0,s}\boldsymbol{D}^2 + diag[d_{1,s}]_d D + diag[d_{2,s}]_d,
\end{array}\right\} \tag{25}$$

and $[\cdots]_d$ is a diagonal matrix.

5. Validation of results

We have solved the modeled equations using the SQLM. To show the convergence of the SQLM numerical scheme, the solution errors have been considered. The solution errors are defined as the difference between the approximate values of the functions at two successive iterations. The infinity norms are used to show the convergence of the SQLM. The infinity norms are defined by:

$$\left.\begin{array}{l}
E_f = \max_{0\le m\le N_x} \|f_{s+1,m} - f_{s,m}\|_\infty, \\
E_\theta = \max_{0\le m\le N_x} \|\theta_{s+1,m} - \theta_{s,m}\|_\infty, \\
E_\sigma = \max_{0\le m\le N_x} \|\sigma_{s+1,m} - \sigma_{s,m}\|_\infty, \\
E_\chi = \max_{0\le m\le N_x} \|\chi_{s+1,m} - \chi_{s,m}\|_\infty.
\end{array}\right\} \tag{26}$$

Again, we check the accuracy of the SQLM by considering the residual error norm at infinity for each function. The infinity norm is determined by substituting the approximate solutions into the differential Eqs. (7)–(8). The norms are defined as:

$$\left.\begin{array}{l}
\|Res\ (f)\|_\infty = \|H_1(2f'^2 - ff'') - H_2 f''' + MH_5 f' - \kappa^2 U_{hs}\exp(-\kappa\eta) - \lambda(H_3\theta - Nr\sigma - Rb\chi)\|_\infty \\
\|Res\ (\theta)\|_\infty = \|H_4 Pr(f'\theta - f\theta') - (H_5 + Rn\ Pr)\theta'' - NbPr\theta'\sigma' - NtPr\theta'^2\|_\infty, \\
\|Res\ (\sigma)\|_\infty = \|Nb\ Le\ (f'\sigma - f\sigma') - Nb\sigma'' - Nt\theta''\|_\infty, \\
\|Res\ (\chi)\|_\infty = \|Lb(f'\chi - f\chi') - \chi'' + Pe[(\chi+\delta)\sigma'' + \chi'\sigma']\|_\infty.
\end{array}\right\} \tag{27}$$

Table 2 present the solution errors of E_f, E_θ, E_σ, and E_χ computed using the SQLM at different iterations level. The error norm in each of the functions is observed to decrease as the number of iterations increases. This shows that the SQLM numerical method converges quickly as the error is observed to reduce prodressively with an increase in the number of iterations.

Table 3 show the residual error varied against the number of iterations. We observe from the table that the residual error decreases as the number of iterations increase. The norm of

Table 2. Convergence of $f(\eta)$, $\theta(\eta)$, $\sigma(\eta)$, and $\chi(\eta)$.

Iterations	E_f	E_θ	E_σ	E_χ
1	7.825×10^{-2}	4.980×10^{-2}	4.073×10^{-2}	3.528×10^{-1}
2	2.039×10^{-2}	1.323×10^{-3}	8.148×10^{-4}	6.952×10^{-3}
3	5.169×10^{-4}	1.157×10^{-5}	3.909×10^{-5}	8.802×10^{-5}
4	2.195×10^{-7}	7.326×10^{-9}	2.946×10^{-8}	2.890×10^{-8}
5	1.047×10^{-10}	1.140×10^{-12}	3.089×10^{-12}	9.353×10^{-12}
6	3.138×10^{-11}	4.873×10^{-12}	2.240×10^{-12}	1.159×10^{-12}
7	8.363×10^{-11}	2.920×10^{-12}	6.711×10^{-12}	7.646×10^{-12}
8	1.555×10^{-11}	9.479×10^{-13}	7.894×10^{-13}	5.264×10^{-12}
9	2.516×10^{-11}	3.432×10^{-13}	9.032×10^{-13}	8.502×10^{-12}
10	1.380×10^{-11}	3.789×10^{-13}	4.876×10^{-13}	4.019×10^{-12}

Table 3. Residual errors for Eqs. (8)–(11).

Iterations	$\|Res\ (f)\|_\infty$	$\|Res\ (\theta)\|_\infty$	$\|Res\ (\sigma)\|_\infty$	$\|Res\ (\chi)\|_\infty$
1	3.138×10^{-2}	2.422×10^{-2}	3.100×10^{-3}	1.863×10^{-1}
2	2.237×10^{-5}	7.918×10^{-5}	1.924×10^{-5}	3.019×10^{-4}
3	1.297×10^{-8}	1.686×10^{-8}	5.694×10^{-9}	1.741×10^{-8}
4	4.483×10^{-11}	8.383×10^{-12}	1.077×10^{-11}	2.491×10^{-11}
5	1.008×10^{-11}	1.046×10^{-12}	8.088×10^{-11}	1.952×10^{-11}
6	1.726×10^{-11}	6.535×10^{-12}	8.178×10^{-12}	1.414×10^{-11}
7	3.604×10^{-11}	7.428×10^{-12}	5.289×10^{-12}	2.082×10^{-11}
8	8.489×10^{-11}	7.937×10^{-12}	6.170×10^{-12}	1.183×10^{-11}
9	8.269×10^{-11}	9.077×10^{-13}	7.209×10^{-12}	1.907×10^{-12}
10	6.627×10^{-11}	5.861×10^{-13}	9.626×10^{-12}	1.689×10^{-12}

the residual decreasing indicates that the accuracy of the approximate solutions obtained using the SQLM improve with an increase in the number of iterations. Convergence is seen to be achieved as the norm of the residual decreases. The results fom the table further shows that the SQLM is an accurate and robust numerical method for solving nonlinear differential equations.

6. Graphical results and discussion

The findings of hybridized NF on an exponentially stretching sheet in the presence of a MHDs, electroosmosis, and radiation effects are investigated in this section. Figure 2 is presented for the flow chart of presented numerical scheme. The physical structures of the plotted figures (Figures 3–27) and true mechanism of flow impressed by the dominant dimensionless parameters are also exposed in this section. All the figures have been plotted in two cases such as mono NF (MoS_2/H_2O) and hybrid NF (SiO_2-MoS_2/H_2O). For the current analysis, the physical parameters have been considered as $L = 30, N_x = 100, \kappa = 1, Lb = 1, U_{hs} = 1, M = 2, Nr = 1, Rb = 1, \phi_1 = 0.1, \phi_2 = 0.3, Nb = 1, Nt = 1, Bi = 0.1, Rn = 1, Le = 1, Pe = 1, Lb = 1, \delta = 1, \lambda = 1,$ and $Pr = 7$. Figures 3–6 display the mixed convection effects on the velocity, temperature, concentration, and motile microorganism distributions. It is noted that, the velocity upsurges with enhancing mixed convection parameter, while temperature, concentration, and motile microorganism are decreasing functions of mixed convection parameter. Moreover, it is noticed from Figures 3 and 4 that, the highest velocities and temperatures are found in case of hybrid NF case as compared with mono NF, and the reverse trend is noticed for concentration and motile microorganism distributions (see Figures 5 and 6). The effects of Hartmann number on the velocity, temperature, concentration, and motile microorganism distributions have been plotted in Figures 7–10. It is clear from Figure 7 that, with enhancing Hartmann number, the velocity declines. When the Hartmann number is high, it means that the magnetic force is relatively strong compared to the viscous force. In this situation, the fluid is effectively pinned by the magnetic field, which suppresses any fluid motion perpendicular to the direction

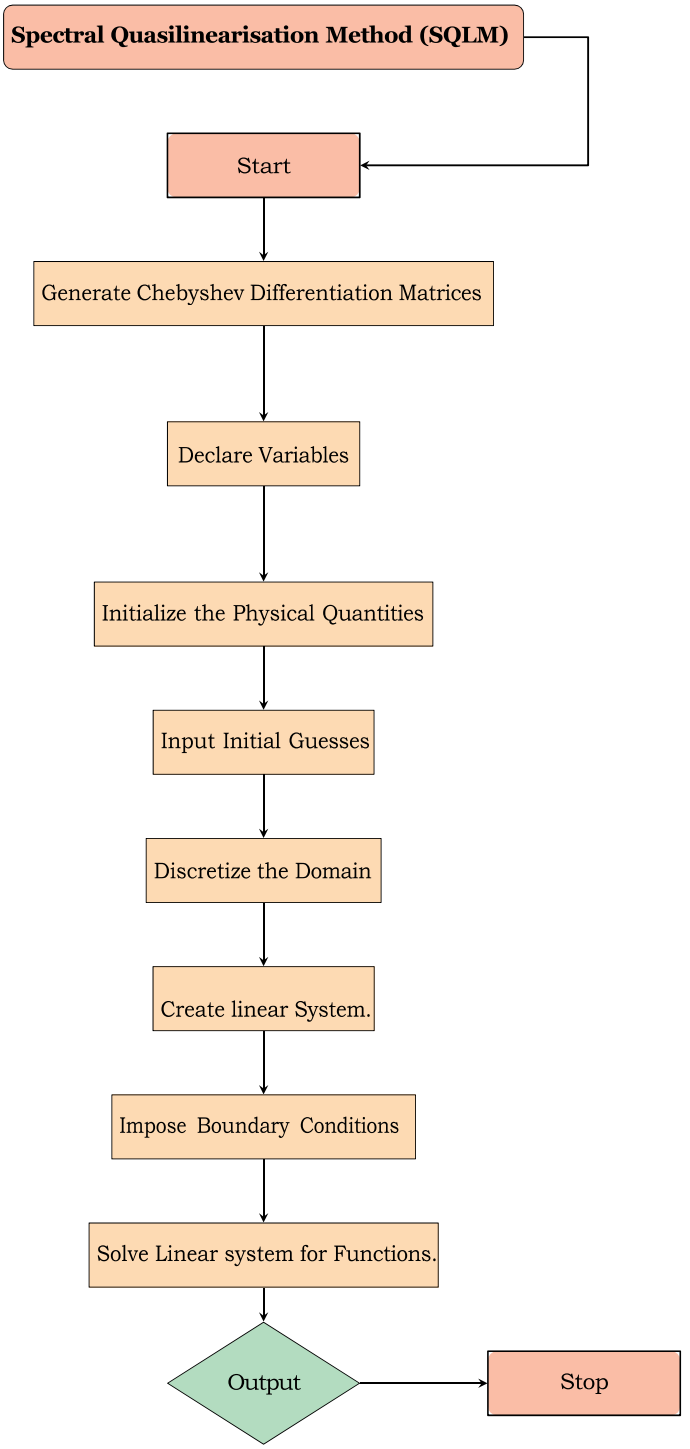


Figure 2. Flow chart of the presented scheme.

of the magnetic field. The temperature, concentration, and motile microorganism are increasing functions of Hartmann number (see Figures 8–10). As the Hartmann number increases, the magnetic field becomes stronger relative to the viscous forces acting on the fluid. This can lead to a

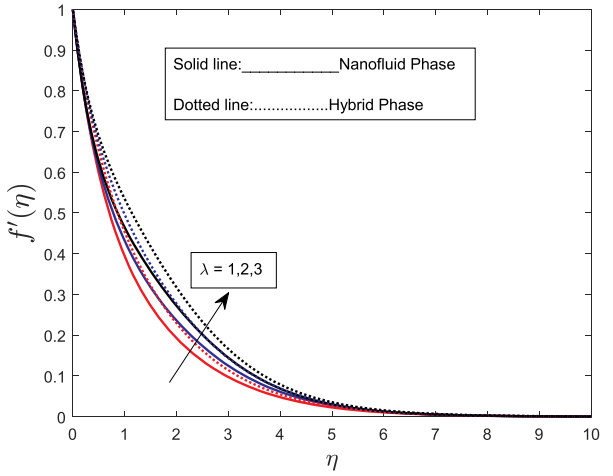


Figure 3. Variation of $f'(\eta)$ with λ.

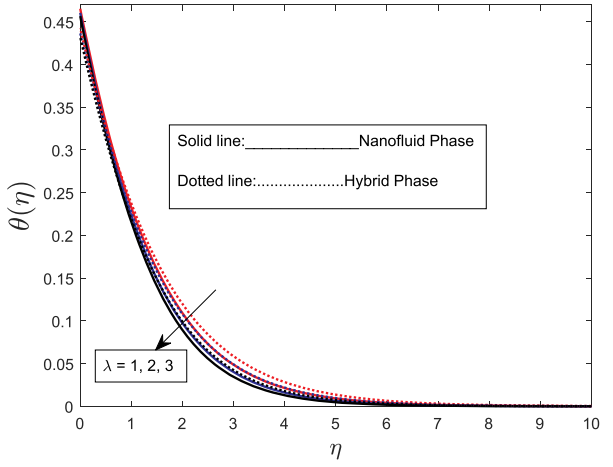


Figure 4. Variation of $\theta(\eta)$ with λ.

decrease in fluid velocity and an increase in the fluid's resistance to flow. As the fluid's resistance to flow increases, more work is required to move the fluid through the system, which can cause an increase in the fluid temperature due to the conversion of work into heat.

Figures 11–13 have been plotted to see the influence of buoyancy ratio constant on the velocity, temperature, and concentration profiles. The velocity is a decreasing function of buoyancy ratio constant (see Figure 11), and the trend is reversed for temperature, and concentration profiles (see Figures 12 and 13). It is clear from the figures that, the higher velocities and temperatures are observed in hybrid NF model as compared with mono NF model, while the reverse trend is seen in concentration profile. The bioconvection Rayleigh constant enhances the velocity profile (see Figure 14), while it declines the concentration profile (see Figure 15). Moreover. The higher velocities are noticed in hybrid NF model, and higher concentrations are found in mono NF model. It is depicted from Figure 16 that, concentration Lewis parameter declines the concentration of NF, and the higher concentration is noted in mono NF as compared with hybrid NF. Figure 17 is plotted to see the variation in temperature with respect to Biot number. It is observed that, with escalating the values of Biot number the temperature escalates. Moreover, the higher temperature is observed in hybrid NF model as compared with mono NF model.

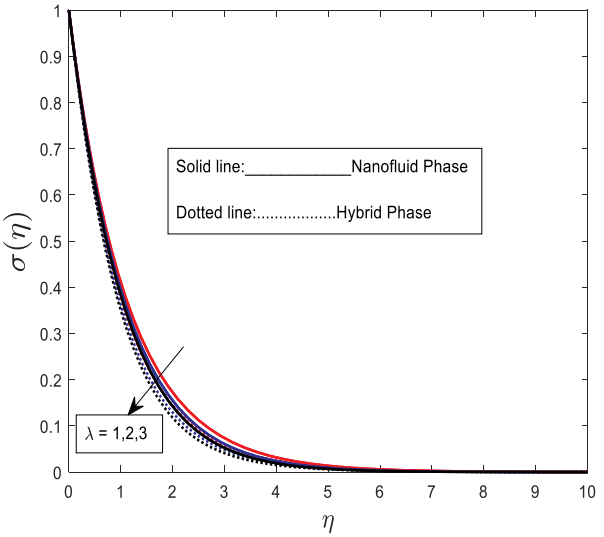


Figure 5. Variation of $\sigma(\eta)$ with λ.

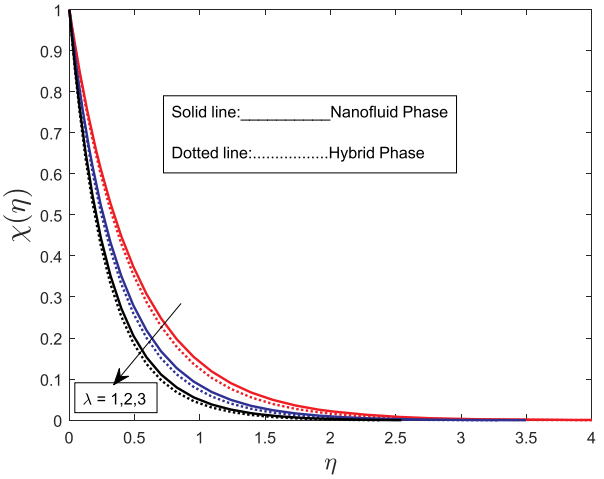


Figure 6. Variation of $\chi(\eta)$ with λ.

Figure 18 is prepared to see the concentration variation with Biot number, and it is observed that the concentration enhances with rising values of Biot number. Moreover, the higher concentration is found for mono NF model. Bioconvection Lewis number effects on the concentration and motile microorganism profiles have been plotted in Figures 19 and 20. From these figures it is noticed that, the concentration is an increasing function of Bioconvection Lewis number, while the motile microorganism is a decreasing function of Bioconvection Lewis number. The higher concentration and motile microorganism can be seen in mono NF. The Peclet number effects on the concentration and motile microorganism have been prepared in Figures 21 and 22. It is noted that, with raising the values of Peclet number tend to decrease the concentration and motile microorganism profiles. Figures 23 and 24 have been plotted to see the effects of thermophoresis parameter on the temperature and concentration of the fluid. It is observed from these figures that both the temperature and concentration profiles are increasing functions of thermophoresis parameter. The higher temperature is found in hybrid NF model and higher concentration is found in mono NF model. It is noted from Figure 25 that, the temperature enhances with raising

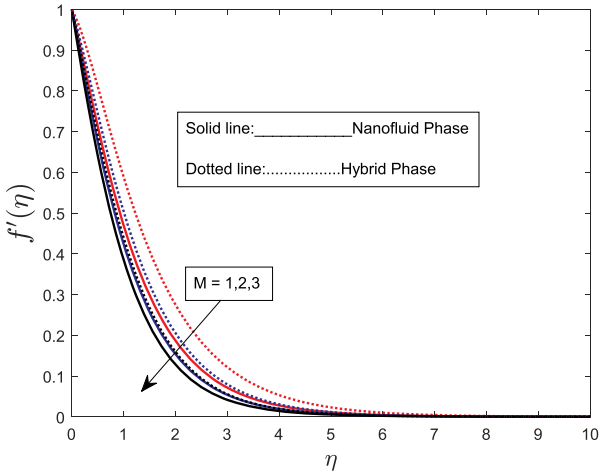


Figure 7. Variation of $f'(\eta)$ with M.

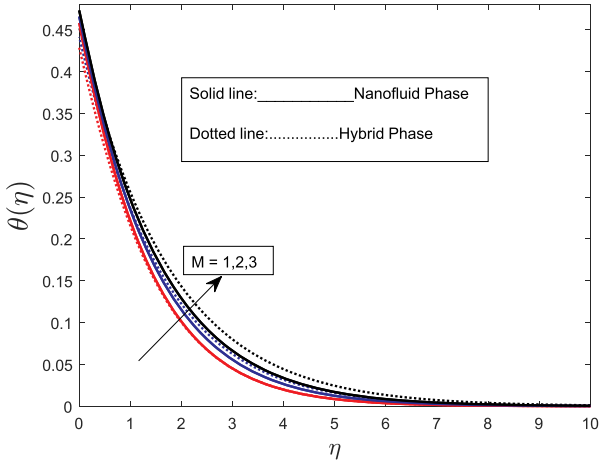


Figure 8. Variation of $\theta(\eta)$ with M.

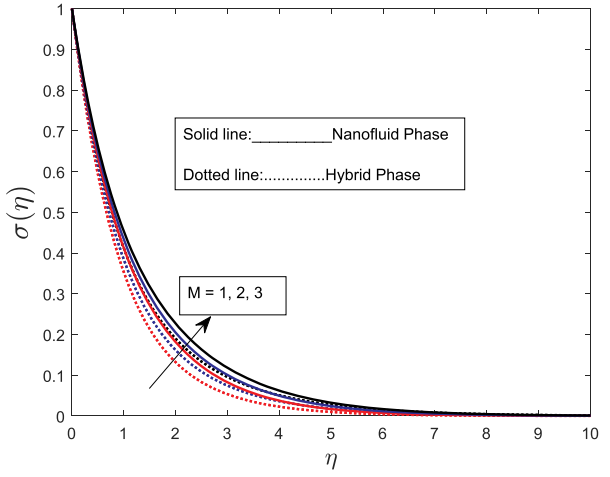


Figure 9. Variation of $\sigma(\eta)$ with M.

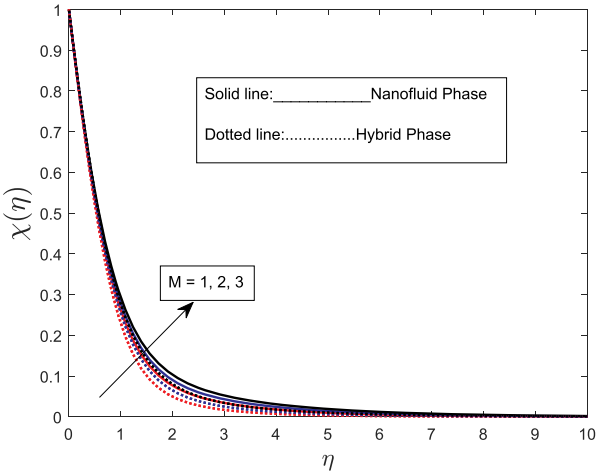


Figure 10. Variation of $\chi(\eta)$ with *M*.

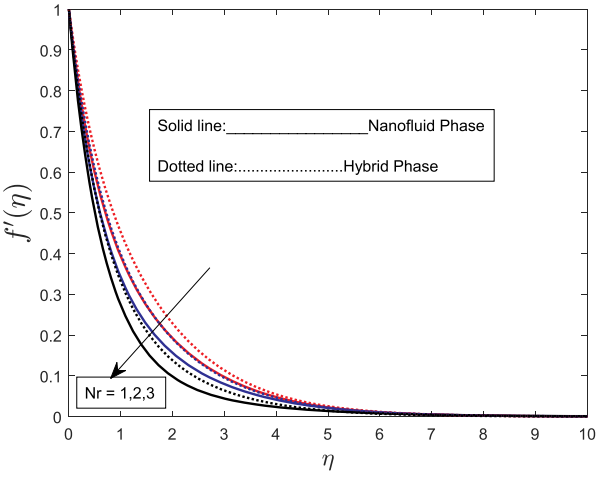


Figure 11. Variation of $f'(\eta)$ with *Nr*.

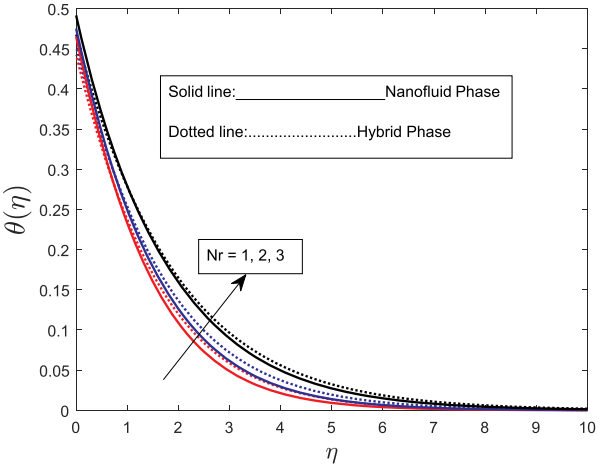


Figure 12. Variation of $\theta(\eta)$ with *Nr*.

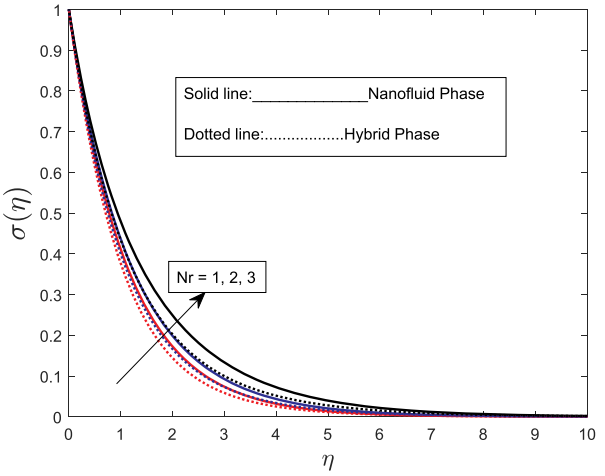


Figure 13. Variation of $\sigma(\eta)$ with *Nr*.

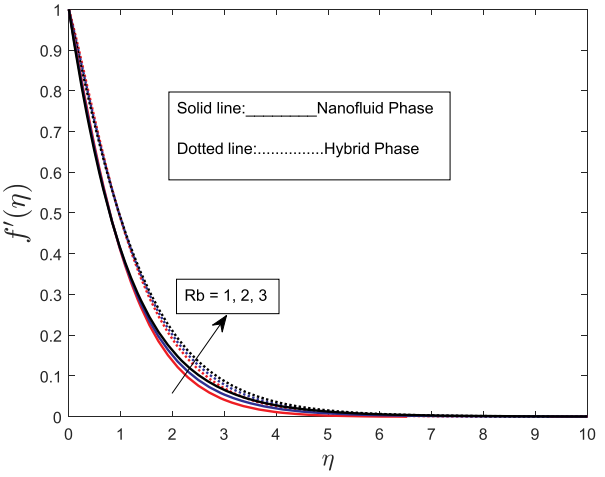


Figure 14. Variation of $f'(\eta)$ with *Rb*.

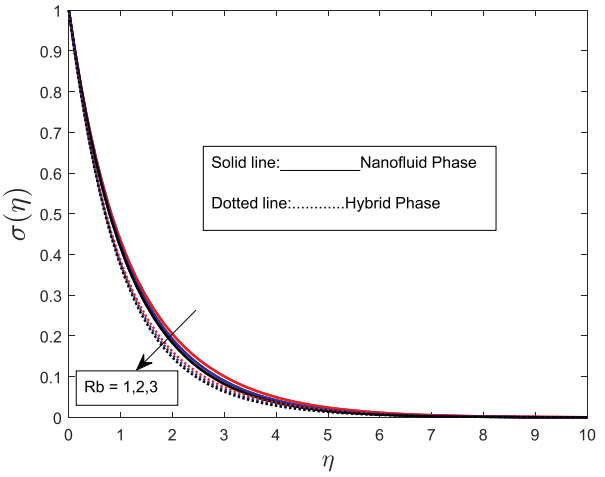


Figure 15. Variation of $\sigma(\eta)$ with *Rb*.

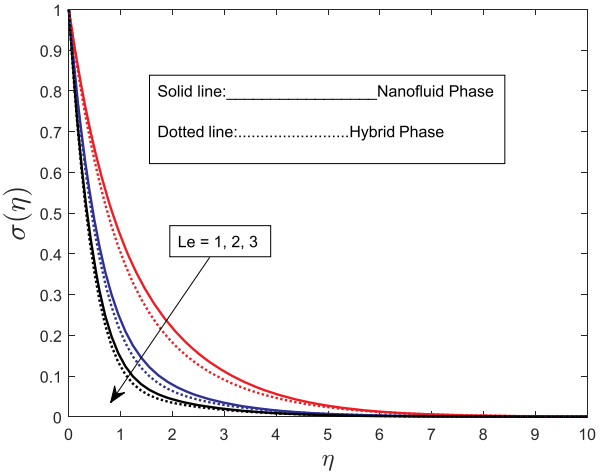


Figure 16. Variation of $\sigma(\eta)$ with *Le*.

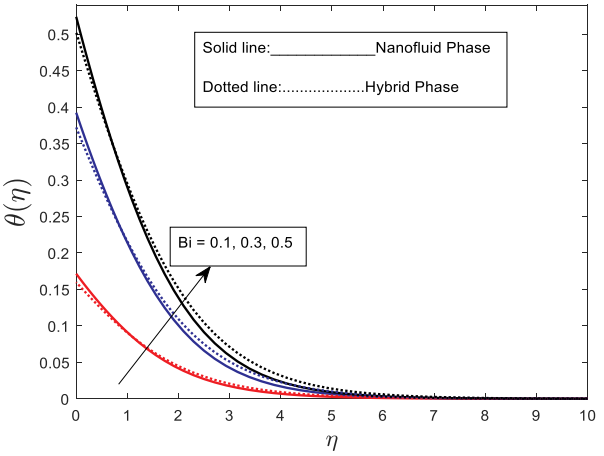


Figure 17. Variation of $\theta(\eta)$ with *Bi*.

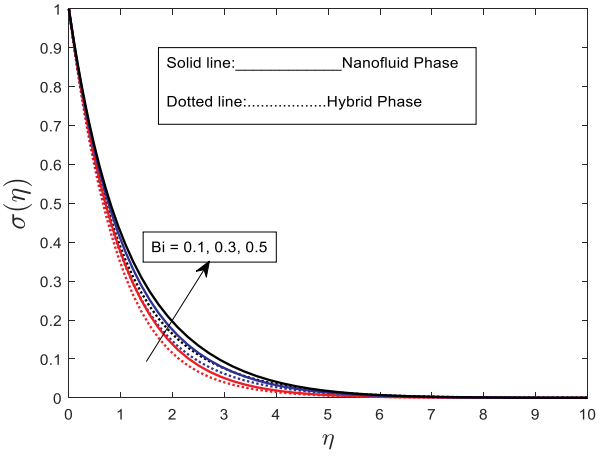


Figure 18. Variation of $\sigma(\eta)$ with *Bi*.

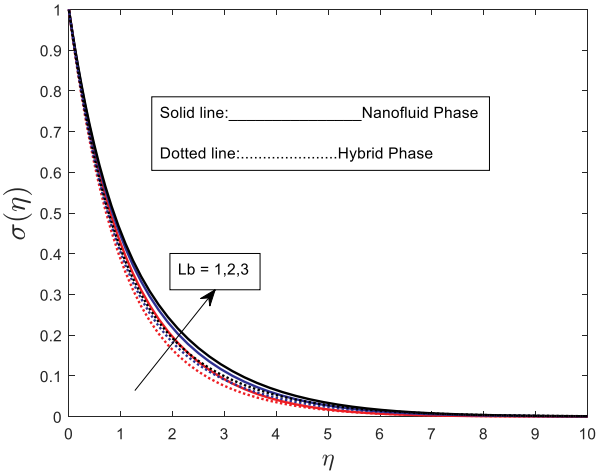


Figure 19. Variation of $\sigma(\eta)$ with *Lb*.

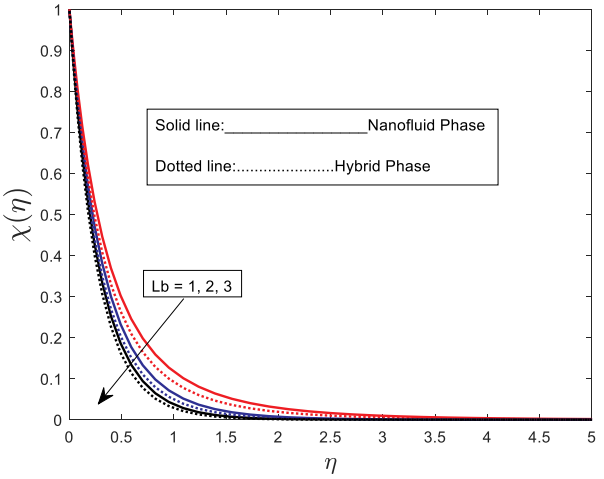


Figure 20. Variation of $\chi(\eta)$ with *Lb*.

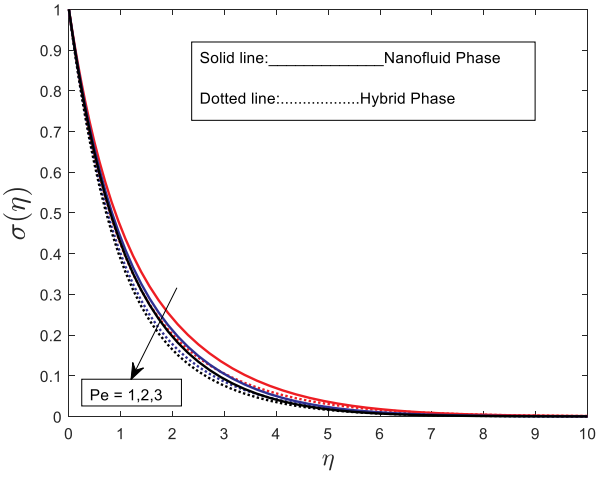


Figure 21. Variation of $\sigma(\eta)$ with *Pe*.

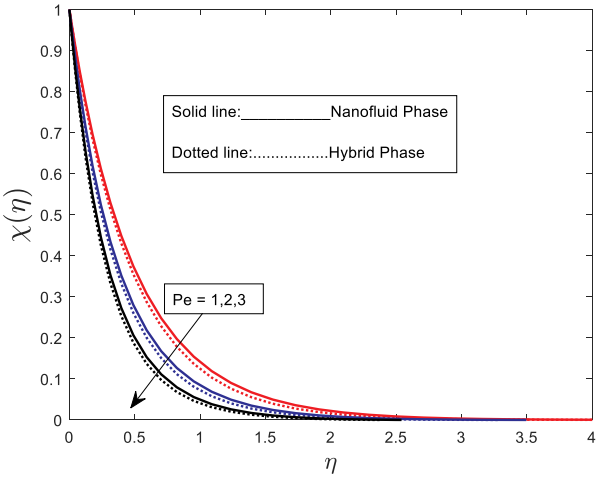


Figure 22. Variation of $\chi(\eta)$ with *Pe*.

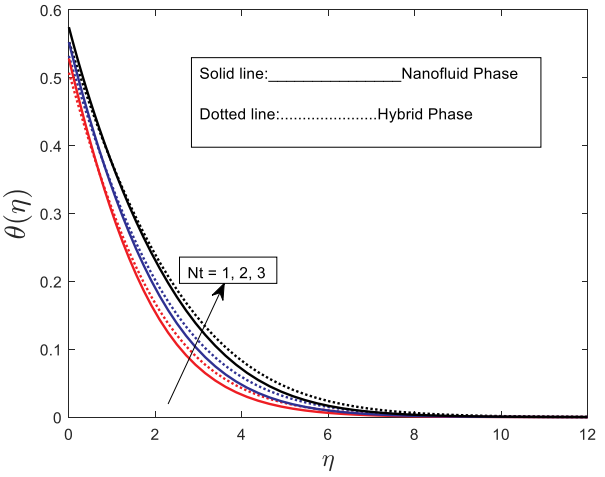


Figure 23. Variation of $\theta(\eta)$ with *Nt*.

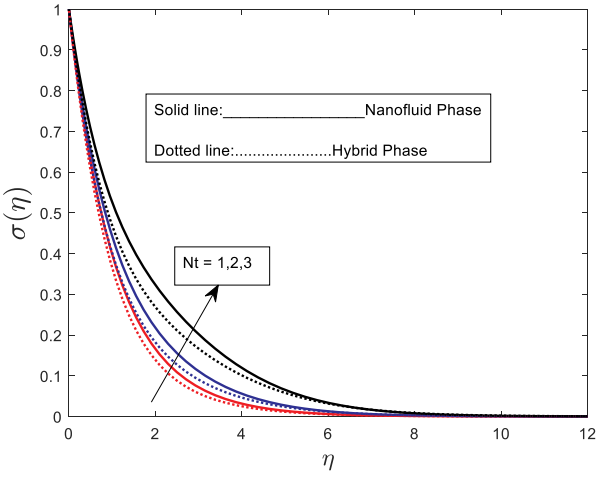


Figure 24. Variation of $\sigma(\eta)$ with *Nt*.

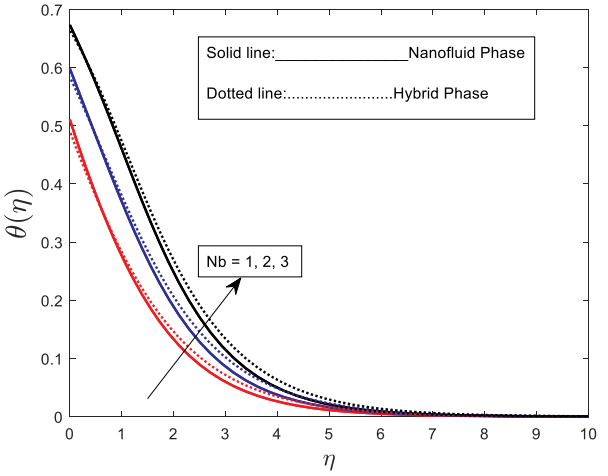


Figure 25. Variation of $\theta(\eta)$ with *Nb*.

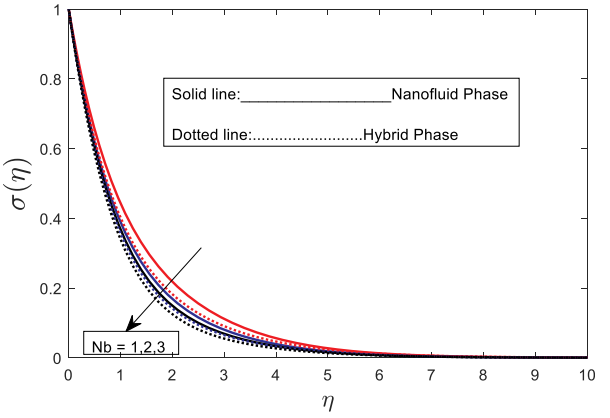


Figure 26. Variation of $\sigma(\eta)$ with *Nb*.

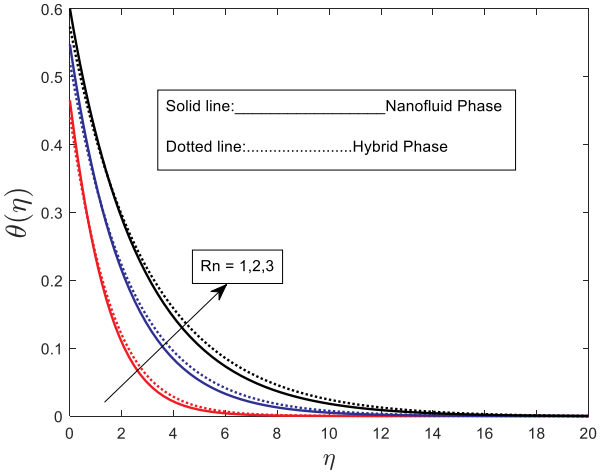


Figure 27. Variation of $\theta(\eta)$ with *Rn*.

Table 4. Numerical values of $\sqrt{\mathrm{Re}_x}\ Cf_x$ and $Nu_x/\sqrt{\mathrm{Re}_x}$ for different values of κ, M, λ, Nr, and Rb.

κ	M	λ	Nr	Rb	$\sqrt{\mathrm{Re}_x}\ Cf_x$	$Nu_x/\sqrt{\mathrm{Re}_x}$
1	2	1	1	1	−4.267436	0.081683
3					−2.675801	0.082376
4					−1.786287	0.082548
5					−0.868499	0.082673
1	1	1	1	1	−3.888659	0.082220
	3				−4.611881	0.081164
	4				−4.929368	0.080660
	5				−5.225076	0.080170
1	2	0.5	1	1	−3.951939	0.081983
		0.8			−4.139574	0.081810
		1.5			−4.599486	0.081310
		2			−4.958390	0.080799
1	2	1	0.5	1	−4.026862	0.082053
			0.7		−4.121132	0.081918
			1		−4.267436	0.081683
			1.5		−4.532114	0.081135
1	2	1	1	2	−4.493724	0.081698
				3	−4.727460	0.081671
				4	−4.968050	0.081616
				5	−5.215716	0.081538

Table 5. Numerical values of $\sqrt{\mathrm{Re}_x}\ Cf_x$ and $Nu_x/\sqrt{\mathrm{Re}_x}$ for different values of Rn, Nb, Nt, Le, and Bi.

Rn	Nb	Nt	Le	Bi	$\sqrt{\mathrm{Re}_x}\ Cf_x$	$Nu_x/\sqrt{\mathrm{Re}_x}$
1	1	1	1	0.1	−4.267435	0.081683
2					−4.230178	0.076705
3					−4.199789	0.072763
4					−4.174855	0.069555
1	0.5	1	1	0.1	−4.314914	0.084102
	2				−4.219677	0.076049
	3				−4.179091	0.069990
	4				−4.140912	0.064086
1	1	0.1	1	0.1	−4.239206	0.082185
		0.5			−4.251505	0.081965
		0.7			−4.257797	0.081853
		2			−4.301747	0.081098
1	1	1	2	0.1	−4.080131	0.080530
			3		−3.989150	0.079773
			4		−3.931189	0.079230
			5		−3.889717	0.078813
1	1	1	1	0.2	−4.236463	0.137263
				0.3	−4.212614	0.177009
				0.4	−4.193879	0.206649
				0.5	−4.178857	0.229519

values of Brownian motion parameter, and the higher temperature is depicted in hybrid NF model. The concentration is a decreasing function of Brownian motion parameter (see Figure 26). Moreover, the higher concentration is noticed in mono NF model as compared with hybrid NF model. Figure 27 is prepared to see the temperature profile for radiation parameter and noted that the temperature increases with an incremental values of radiation parameter. It is also noted that, the higher temperatures are observed in hybrid NF model as compared with single NF model.

Tables 4 and 5 have been prepared to see the variations in LNN and SFC with various involved parameters. It is observed that, SFC and LNN are increasing functions of the electroosmosis parameter. An increase in the electroosmosis parameter may imply higher fluid motion and interaction with the surface, leading to increased skin friction and local Nusselt number. Both SFC and LNN decrease with enhancing values of the parameters such as Hartmann number, mixed convection parameter, buoyancy ratio constant, and bioconvection Rayleigh constant.

Table 6. Comparison of $-\theta'(0)$ with previously published work of Grubka and Bobba [46], when $H_4 = 1$, in the absence of H_5, Nb, Nt, Bi, and Rn.

Pr	Ref. [46]	Present
0.01	−0.0197	−0.0197
0.72	−0.8086	−0.8086
1.00	−1.0000	−1.0000
3.00	−1.9237	−1.9237
10.00	−3.7207	−3.7207
100.00	−12.2940	−12.2940

Radiation parameter enhances SFC and declines the local Nusselt number. An increase in the radiation parameter implies a stronger influence of radiation heat transfer. Radiation tends to contribute to surface heating, which can lead to higher skin friction and reduced heat transfer (lower local Nusselt number). increasing Brownian motion parameter raises SFC and declines LNN. An increase in Brownian motion parameter may lead to more collisions with the surface, contributing to higher skin friction and reduced local Nusselt number. SFC and LNN are decreasing functions of thermophoresis parameter. A decrease in thermophoresis parameter suggests less particle motion, leading to lower skin friction and increased local Nusselt number. Lewis number enhances SFC and deduces LNN, while SFC and LNN are increasing functions of Biot number. An increase in Lewis number suggests a greater influence of thermal diffusion, leading to higher skin friction and decreased local Nusselt number. Higher Biot number indicates a more dominant external heat transfer, contributing to increased skin friction and local Nusselt number. Table 6 represents that comparison of the current study with the existing literature Grubka and Bobba [46]. It is noted from this table that the current results are in close agreement with the existing literature.

7. Conclusions

The current study focuses on the flow of a silica-molybdenum disulfide/water hybrid nanoliquid over an exponentially stretching sheet. This flow is subjected to the effects of electroosmosis, a magnetic field, and thermal radiation. The study employs the modified Buongiorno NF model to analyze and understand the behavior of this complex system. The complex set of differential equations have been simplified under the similarity transformations and non-dimensional entities. To investigate the model, the well established SQLM has been implemented. The important findings of the present investigation are:

- Under the application of stronger buoyancy ratio and magnetic field the velocity is declined.
- There is an enhancement in temperature with raising values of radiation parameter, Hartmann number, buoyancy ratio and Biot number.
- The concentration is an increasing function of Hartmann number, thermophoresis parameter, and bioconvection Lewis number.
- The Peclet number and mixed convection parameter decline the motile microorganism profile.
- The SFC enhances with incremental values of electroosmosis, radiation, and Brownian motion parameters.
- The local Nusselt number declines with Hartmann and Lewis numbers.

NF flows over stretching sheets are an important research area with significant potential for future research. Some possible future research directions in this field could include: The use of advanced numerical methods, such as artificial neural networks, machine learning, or deep learning, could be explored in future studies to improve the accuracy and efficiency of simulations of NF flows over stretching sheets.

Authors' contribution

MDS: formulation and simulations, TMA: draft preparation, KKA: analysis of results. KR: validation and supervision.

Disclosure statement

The authors declare that they have no known competing financial interests or personal relationships that could have appeared to influence the work reported in this article.

Ethical approval

Not applicable.

Funding

Not applicable.

ORCID

MD. Shamshuddin http://orcid.org/0000-0002-2453-8492
Katta Ramesh http://orcid.org/0000-0003-3329-508X

Availability of data and materials

No datasets were generated or analyzed during the current study.

References

[1] S. U. S. Choi, "Enhancing thermal conductivity of fluids with nanoparticles, developments and applications of non-Newtonian flows," *ASME*, vol. 231, pp. 99–I05, 1995.
[2] A. Ahmed, M. Khan, J. Ahmed, A. Hafeez, and Z. Iqbal, "Unsteady stagnation point flow of Maxwell nanofluid over stretching disk with joule heating," *Arab. J. Sci. Eng.*, vol. 45, no. 7, pp. 5529–5540, 2020. DOI: 10.1007/s13369-020-04468-9.
[3] M. Usman, R. U. Haq, M. Hamid and W. Wang, "Least square study of heat transfer of water based Cu and Ag nanoparticles along a converging/diverging channel," *J. Mol. Liq.*, vol. 249, pp. 856–867, 2018. DOI: 10.1016/j.molliq.2017.11.047.
[4] S. Anjan and H. Mondal, "Spectral quasilinearization method for Sisko nanofluid past a stretching cylinder with activation energy and entropy generation effects subject to variable thermal conductivity," *Heat Transf.*, vol. 51, no. 8, pp. 7773–7786, 2022. DOI: 10.1002/htj.22665.
[5] M. J. Uddin, O. A. Bég and A. I. Ismail, "Radiative convective nanofluid flow past a stretching/shrinking sheet with slip effects," *J. Thermophys. Heat Transf.*, vol. 29, no. 3, pp. 513–523, 2015. DOI: 10.2514/1.T4372.
[6] M. J. Uddin, N. A. Amirsom, O. A. Bég and A. I. Ismail, "Computation of bio-nano-convection power law slip flow from a needle with blowing effects in a porous medium," *Waves Random Complex Media*, pp. 1–21, 2022, DOI: 10.1080/17455030.2022.2048919.
[7] N. A. Amirsom, M. J. Uddin, M. F. M. Basir, A. I. M. Ismail, O. A. Bég and A. Kadir, "Three-dimensional bioconvection nanofluid flow from a bi-axial stretching sheet with anisotropic slip," *JSM*, vol. 48, no. 5, pp. 1137–1149, 2019. DOI: 10.17576/jsm-2019-4805-23.
[8] A. Raza *et al.*, "Thermal activity of conventional Casson nanoparticles with ramped temperature due to an infinite vertical plate via fractional derivative approach," *Case Stud. Therm. Eng.*, vol. 27, pp. 101191, 2021. DOI: 10.1016/j.csite.2021.101191.
[9] M. J. Uddin, P. Rana, S. Gupta and M. N. Uddin, "Bio-nanoconvective micropolar fluid flow in a Darcy porous medium past a cone with second-order slips and Stefan blowing: FEM solution," *Iran J. Sci. Technol. Trans. Mech. Eng.*, vol. 47, no. 4, pp. 1633–1647, 2023. DOI: 10.1007/s40997-023-00626-0.

[10] T. Z. Fatema, M. J. Uddin, M. F. Basir and A. I. M. Ismail, "Magnetohydrodynamic bio-nano-convective slip flow with Stefan blowing effects over a rotating disc," *Proc. Inst. Mech. Eng. N J. Nanomater. Nanoeng. Nanosyst.*, vol. 234, no. 3-4, pp. 83–97, 2020. DOI: 10.1177/2397791419881580.

[11] J. Buongiorno, "Convective transport in nanofluids," *J. Heat Transf.*, vol. 128, no. 3, pp. 240–250, 2006. DOI: 10.1115/1.2150834.

[12] J. Rahman, *et al.*, "Numerical simulation of Darcy–Forchheimer 3D unsteady nanofluid flow comprising carbon nanotubes with Cattaneo–Christov heat flux and velocity and thermal slip conditions," *Processes*, vol. 7, no. 10, pp. 687, 2019. DOI: 10.3390/pr7100687.

[13] MD. Shamshuddin, S. O. Salawu, K. K. Asogwa and P. Srinivasa Rao, "Thermal exploration of convective transportation of ethylene glycol based magnetized nanofluid flow in porous cylindrical annulus utilizing MOS_2 and Fe_3O_4 nanoparticles with inconstant viscosity," *J. Magn. Magn. Mater.*, vol. 573, pp. 170663, 2023. DOI: 10.1016/j.jmmm.2023.170663.

[14] M. M. Bhatti, H. F. Öztop, R. Ellahi, I. E. Sarris and M. H. Doranehgard, "Insight into the investigation of diamond (C) and Silica (SiO_2) nanoparticles suspended in water-based hybrid nanofluid with application in solar collector," *J. Mol. Liq.*, vol. 357, pp. 119134, 2022. DOI: 10.1016/j.molliq.2022.119134.

[15] B. Ruhani, P. Barnoon and D. Toghraie, "Statistical investigation for developing a new model for rheological behavior of Silica–ethylene glycol/Water hybrid Newtonian nanofluid using experimental data," *Phys. A Stat. Mech. Appl.*, vol. 525, pp. 616–627, 2019. DOI: 10.1016/j.physa.2019.03.119.

[16] N. Iftikhar, A. Rehman and H. Sadaf, "Theoretical investigation for convective heat transfer on Cu/water nanofluid and (SiO_2-copper)/water hybrid nanofluid with MHD and nanoparticle shape effects comprising relaxation and contraction phenomenon," *Int. Commun. Heat Mass Transf.*, vol. 120, pp. 105012, 2021. DOI: 10.1016/j.icheatmasstransfer.2020.105012.

[17] P. M. Patil, H. F. Shankar and M. A. Sheremet, "Mixed convection of silica–molybdenum disulphide/water hybrid nanoliquid over a rough sphere," *Symmetry*, vol. 13, no. 2, pp. 236, 2021. DOI: 10.3390/sym13020236.

[18] F. Ali, M. Gohar, I. Khan, N. A. Sheikh, S. A. A. Jan and M. Saqib, "Magnetite molybdenum disulphide nanofluid of grade two: a generalized model with Caputo-Fabrizio derivative," *Microfluid. Nanofluid.*, vol. 10, pp. 257–276., 2018, DOI: 10.5772/intechopen.72863.

[19] R. S. Varun Kumar, R. J. Punith Gowda, R. Naveen Kumar, M. Radhika and B. C. Prasannakumara, "Two-phase flow of dusty fluid with suspended hybrid nanoparticles over a stretching cylinder with modified Fourier heat flux," *SN Appl. Sci.*, vol. 3, no. 3, pp. 1–9, 2021. DOI: 10.1007/s42452-021-04364-3.

[20] M. Arif, F. Ali, N. A. Sheikh and I. Khan, "Enhanced heat transfer in working fluids using nanoparticles with ramped wall temperature: applications in engine oil," *Adv. Mech. Eng.*, vol. 11, no. 11, pp. 168781401988098, 2019. DOI: 10.1177/1687814019880987.

[21] A. Gul, I. Khan and S. S. Makhanov, "Entropy generation in a mixed convection Poiseulle flow of molybdenum disulphide Jeffrey nanofluid," *Results Phys.*, vol. 9, pp. 947–954, 2018. DOI: 10.1016/j.rinp.2018.03.012.

[22] S. Shafie, A. Gul and I. Khan, "Molybdenum disulfide nanoparticles suspended in water-based nanofluids with mixed convection and flow inside a channel filled with saturated porous medium," AIP Conf. Proc., vol. 1775, 2016. pp. 030042, DOI: 10.1063/1.4965162.

[23] Y. Zhang, S. Gu, B. Yan and J. Ren, "Solvent-free ionic molybdenum disulphide (MoS_2) nanofluids," *J. Mater. Chem.*, vol. 22, no. 30, pp. 14843–14846, 2012. DOI: 10.1039/c2jm33106c.

[24] M. I. Khan, S. A. Khan, T. Hayat, M. Waqas and A. Alsaedi, "Modeling and numerical simulation for flow of hybrid nanofluid ($SiO_2/C_3H_8O_2$) and ($MoS_2/C_3H_8O_2$) with entropy optimization and variable viscosity," *HFF*, vol. 30, no. 8, pp. 3939–3955, 2020. DOI: 10.1108/HFF-10-2019-0756.

[25] M. Saqib, F. Ali, I. Khan, N. A. Sheikh and S. B. Shafie, "Convection in ethylene glycol-based molybdenum disulfide nanofluid: Atangana–Baleanu fractional derivative approach," *J. Therm. Anal. Calorim.*, vol. 135, no. 1, pp. 523–532, 2019. DOI: 10.1007/s10973-018-7054-9.

[26] A. Talha, P. Kumam, P. Thounthong and K. Sitthithakerngkiet, "Nanoparticles shape effects on thermal performance of Brinkman-type ferrofluid under heat injection/consumption and thermal radiation: a fractional model with non-singular kernel and non-uniform temperature and velocity conditions," *J. Mol. Liq.*, vol. 335, pp. 116107, 2021. DOI: 10.1016/j.molliq.2021.116107.

[27] J. Liu, G. M. Choi and D. G. Cahill, "Measurement of the anisotropic thermal conductivity of molybdenum disulfide by the time-resolved magneto-optic Kerr effect," *J. Appl. Phys*, vol. 116, no. 23, pp. 233107, 2014. DOI: 10.1063/1.4904513.

[28] I. Khan, "Shape effects of MoS2 nanoparticles on MHD slip flow of molybdenum disulphide nanofluid in a porous medium," *J. Mol. Liq*, vol. 233, pp. 442–451, 2017. DOI: 10.1016/j.molliq.2017.03.009.

[29] S. M. Hussain, "Dynamics of radiative Williamson hybrid nanofluid with entropy generation: significance in solar aircraft," *Sci. Rep.*, vol. 12, no. 1, pp. 8916, 2022. DOI: 10.1038/s41598-022-13086-4.

[30] B. Takabi and S. Salehi, "Augmentation of the heat transfer performance of a sinusoidal corrugated enclosure by employing hybrid nanofluid," *Adv. Mech. Eng.*, vol. 6, pp. 147059, 2014. DOI: 10.1155/2014/147059.

[31] S. Suresh, K. Venkitaraj, P. Selvakumar and M. Chandrasekar, "Synthesis of Al_2O_3-cu/water hybrid nanofluids using two step method and its thermo physical properties," *Colloids Surf. A*, vol. 388, no. 1–3, pp. 41–48, 2011. DOI: 10.1016/j.colsurfa.2011.08.005.

[32] D. Khan, P. Kumam, I. Khan, A. Khan, W. Watthayu and M. Arif, "Scientific investigation of a fractional model based on hybrid nanofluids with heat generation and porous medium: applications in the drilling process," *Sci. Rep.*, vol. 12, no. 1, pp. 6524, 2022. DOI: 10.1038/s41598-022-10398-3.

[33] T. H. Al-Arabi, A. Mahdy, A. M. Rashad, W. Saad and H. A. Nabwey, "Convective flow of a Williamson hybrid nanofluid in a porous medium through a cone and wedge with the effect of the shape of nanoparticles," *Heat Transf.*, vol. 51, no. 8, pp. 7009–7029, 2022. DOI: 10.1002/htj.22634.

[34] S. U. Devi and S. P. A. Devi, "Numerical investigation of three-dimensional hybrid Cu-Al_2O_3/water nanofluid flow over a stretching sheet with effecting Lorentz force subject to Newtonian heating," *Can. J. Phys.*, vol. 94, no. 5, pp. 490–496, 2016. DOI: 10.1139/cjp-2015-0799.

[35] S. L. Sundar, M. K. Singh and A. C. Sousa, "Enhanced heat transfer and friction factor of MWCNT-Fe_3O_4/water hybrid nanofluids," *Int. Commun. Heat Mass Transf.*, vol. 52, pp. 73–83, 2014. DOI: 10.1016/j.icheatmasstransfer.2014.01.012.

[36] A. Talha, P. K. Asifa and K. Sitthithakerngkiet, "A fractional model for thermal investigation of MoS_2-Fe_3O_4/engine oil hybrid nanofluid under double ramped conditions and shape factor influence: the Atangana–Baleanu approach," *Math. Methods Appl. Sci.*, 2021. DOI: 10.1002/mma.7756.

[37] Asifa, T. Anwar, P. Kumam, and S. Muhammad, "New fractional model to analyze impacts of Newtonian heating, shape factor and ramped flow function on MgO-SiO_2-Kerosene oil hybrid nanofluid," *Case Stud. Therm. Eng.*, vol. 38, pp. 102361, 2022. DOI: 10.1016/j.csite.2022.102361.

[38] Asifa, T. Anwar, P. Kumam, Z. Shah, and K. Sitthithakerngkiet, "Significance of shape factor in heat transfer performance of molybdenum-disulfide nanofluid in multiple flow situations; A comparative fractional study," *Molecules*, vol. 26, pp. 3711, 2021. DOI: 10.3390/molecules26123711.

[39] Asifa, T. Anwar, P. Kumam, M. Y. Almusawa, S. A. Lone, and P. Suttiarporn, "Exact solutions via Prabhakar fractional approach to investigate heat transfer and flow features of hybrid nanofluid subject to shape and slip effects," *Sci. Rep.*, vol. 13, pp. 7810, 2023. DOI: 10.1038/s41598-023-34259-9.

[40] N. Acharya, "Spectral quasi linearization simulation on the hydrothermal behaviour of hybrid nanofluid spraying on an inclined spinning disk," *Partial Differ. Equ. Appl.*, vol. 4, pp. 100094, 2021. DOI: 10.1016/j.padiff.2021.100094.

[41] W. Ibrahim, "Spectral quasilinearization method for solution of convective heating condition," *Eng. Trans.*, vol. 68, pp. 69–87, 2020. DOI: 10.24423/EngTrans.1062.20200102.

[42] M. S. Ansari, V. M. Magagula and M. Trivedi, "Jeffrey nanofluid flow near a Riga plate: spectral quasi linearization approach," *Heat Transf.*, vol. 49, no. 3, pp. 1491–1510, 2021. DOI: 10.1002/htj.21673.

[43] S. Shateyi and H. Muzara, "On numerical analysis of Carreau–Yasuda nanofluid flow over a non-linearly stretching sheet under viscous dissipation and chemical reaction effects," *Mathematics*, vol. 8, no. 7, pp. 1148, 2020. DOI: 10.3390/math8071148.

[44] M. Dhlamini, H. Mondal, P. Sibanda and S. Motsa, "Rotational nanofluids for oxytactic microorganisms with convective boundary conditions using bivariate spectral quasi-linearization method," *J. Cent. South. Univ.*, vol. 27, no. 3, pp. 824–841, 2020. DOI: 10.1007/s11771-020-4334-x.

[45] J. Prakash, M. Ramzan, S. Saleem, A. Verma and K. Ramesh, "Homotopy analysis on the bio-inspired radiative magnesium and iron oxides/blood nanofluid flow over an exponential stretching sheet," *Comp. Part. Mech.*, vol. 10, no. 6, pp. 1955–1975, 2023. DOI: 10.1007/s40571-023-00600-2.

[46] L. J. Grubka and K. M. Bobba, "Heat transfer characteristics of a continuous stretching surface with variable temperature," *J. Heat Transf.* vol. 107, no. 1, pp. 248–250, 1985. DOI: 10.1115/1.3247387.